

# Highly Stretchable and Sensitive Pressure Sensor Array Based on Icicle-Shaped Liquid Metal Film Electrodes

Yiqiu Zhang, Sidi Liu, Yihui Miao, Han Yang, Xuyue Chen, Xiang Xiao, Zhongyun Jiang, Xinjian Chen, Baoqing Nie,\* and Jian Liu\*



Cite This: *ACS Appl. Mater. Interfaces* 2020, 12, 27961–27970



Read Online

ACCESS |



Metrics & More



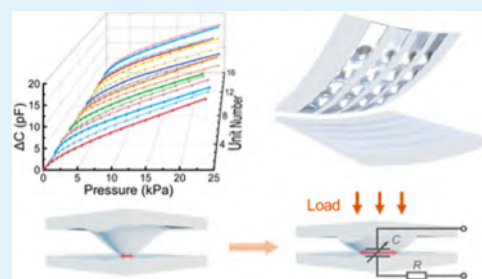
Article Recommendations



Supporting Information

**ABSTRACT:** Flexible pressure sensors emerge for important applications in wearable electronics, with increasing requirements for high sensitivity, fast response, and low detection limit. However, there is still a challenge in this field, that is, how to maximize both the electrical performance and mechanical stretchability simultaneously. Here, we report a straightforward and cost-effective method to fabricate highly stretchable and sensitive capacitive pressure sensor arrays. It features a unique design of integrating the icicle-shaped liquid metal film electrode and reliable processing of the liquid metal and elastomer. Under an external load, the deformation of the elastic bump structure dramatically results in an increase in the overlapping area of the electrodes and a decrease in the separation distance, offering a new capacitive sensing scheme with an enhanced sensitivity. Our sensor has been demonstrated with a high sensitivity of  $39\% \text{ kPa}^{-1}$  in the range of 0–1 kPa, limit of detection as low as 12 Pa, hysteresis error of 8.46% at a maximum pressure of 25 kPa, and stretchability up to 94% strain without any failure. The arrayed sensor has been successfully applied to force measurements on a curved surface, contour mapping of external loads, and monitoring of contact pressures under various cervical postures.

**KEYWORDS:** wearable electronics, capacitance, pressure sensors, liquid metal, biomedical applications



## INTRODUCTION

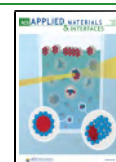
In recent years, with the rapid development of intelligent terminals and Internet of Things (IoT), flexible and stretchable tactile pressure sensing promises a huge market prospect in health monitoring, wearable electronics, and soft robotics.<sup>1–4</sup> There are several categories of technologies to transduce mechanical pressures, including piezoresistive, capacitive, piezoelectric, and optical approaches. Among these, capacitive pressure sensors are attractive due to the advantages of high sensitivity, low power consumption, and compact geometry in construction.<sup>5–7</sup> Most of the capacitive pressure sensors are fabricated as parallel-plate capacitors, featuring a dielectric layer sandwiched by two electrode plates.<sup>8</sup> In such a configuration, elastic polymeric materials, such as soft silicone rubbers, flexible gels, and elastic fabrics, are good candidates for the dielectric layer, considering their excellent stretchability and outstanding flexibility.<sup>9,10</sup> For applications where high sensitivity and fast response are required, many efforts have been devoted to creating microstructures on sensing layers/electrodes or introducing micropores in the bulk of the dielectric layer.<sup>11–14</sup> For example, Cho et al. developed a highly sensitive pressure sensor with micropatterned pyramidal ionic gels sandwiched by ITO/PET electrodes;<sup>13</sup> Kim et al. demonstrated a transparent pressure sensor by dispersing silica beads on the surface of a poly(dimethylsiloxane) (PDMS) dielectric membrane;<sup>14</sup> and Chen et al. developed a method to

control the fragmentation of graphene and designed an ultrathin and highly skin-conformable pressure sensor, taking advantage of the inherent structure of fingerprint.<sup>15,16</sup> Moreover, designs of hierarchical structure can further enhance the sensitivity and dynamic range.<sup>17,18</sup> Another strategy to enhance the sensor performance is to create micropores in the bulk of the sensing layers. The air pores can be introduced into elastomers, thus providing more space for compression and reducing the effective modulus.<sup>8,19–23</sup> Pruvost et al. developed a dielectric layer of porous carbon black/PDMS foam, in which the modulus is effectively reduced by 97.5% and the relative permittivity is significantly increased by 750% due to the presence of air pores and carbon black inside PDMS, respectively,<sup>20</sup> and Kwon et al. fabricated a sensor featuring a microporous dielectric layer, the dynamic range of which (up to 130 kPa) covers almost the entire pressure range from human activity.<sup>22</sup> Chen et al. demonstrated a piezoresistive pressure sensor based on a lightweight polyimide/carbon nanotube composite aerogel with a robust foam structure.<sup>24</sup>

Received: March 16, 2020

Accepted: June 5, 2020

Published: June 5, 2020



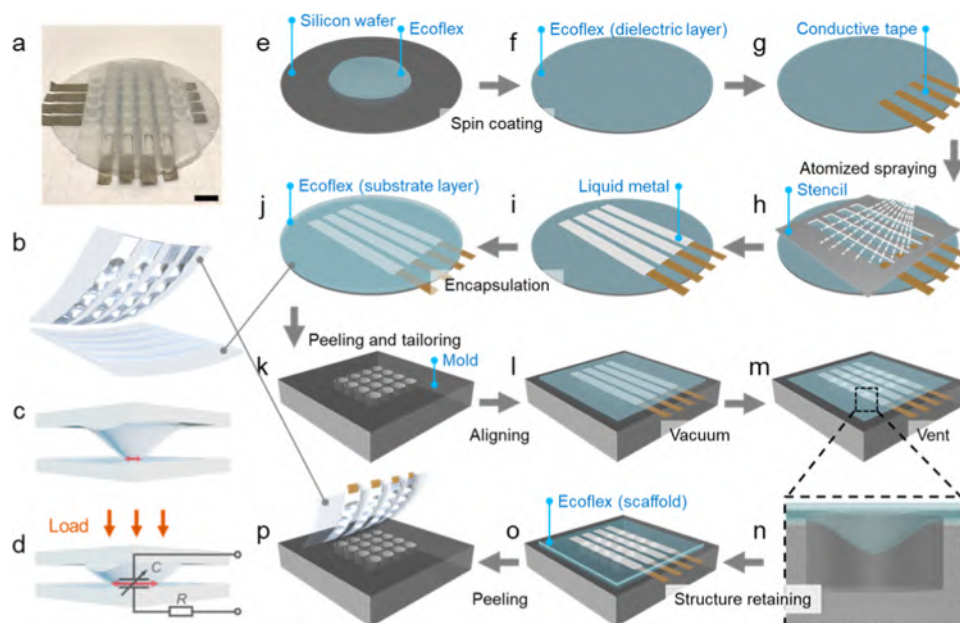


**Figure 1.** Device fabrication. (a) Photograph of the  $4 \times 4$  pressure sensor array. Scale bar: 1 cm. (b) Schematic drawing of the 3D structure of the pressure sensor, featuring a top layer of icicle-shaped film electrode arrays orthogonally onto a bottom layer of the flat film electrode. (c, d) Sketches of a single sensing unit in the cross-sectional view without and with a mechanical load.  $C$  is the force-sensitive capacitance between the top and bottom electrodes.  $R$  is the equivalent resistance of the electrodes. The overlapping area of  $C$  increases largely along with the pressure. (e–j) Schematic diagrams of the fabrication procedure of the bottom liquid metal electrode encapsulated in Ecoflex. (k–p) Fabrication procedure of the top layer of the icicle-shaped liquid metal electrode encapsulated in Ecoflex.

Soft electrodes have actively been developed by blending conductive fillers, such as carbon nanotubes, metal particles, nanowires, and graphene-based materials, into polymer matrices such as PDMS, styrene–ethylene–butylene–styrene (SEBS), and polyurethane (PU).<sup>25–29</sup> The sensitivity of capacitive pressure sensors can be significantly improved by modifying three-dimensional structures on the surface of such elastic electrodes.<sup>29,30</sup> However, the incorporation of rigid particles into soft polymers could increase the stiffness and sacrifice the durability and stretchability of the electrode. Unfortunately, a sharp and irreversible increase of resistance may occur when the electrodes are bent or stretched with the risk of device failure.<sup>31,32</sup> Compared with these composite materials, a gallium (Ga)-based liquid metal offers a new option for soft electrodes, which is intrinsically fluidic and highly conductive at room temperature.<sup>33</sup> Liquid metal-based electrodes have excellent stretchability (up to 700% strain) while maintaining the metallic conductivity.<sup>34,35</sup> In addition, Ga-based liquid metals are biocompatible, thus with the potential of being applied to disease therapies, including light-driven drug delivery,<sup>36</sup> conformable skin tumor photothermal therapy,<sup>37</sup> and implantable electrodes for nerve connection.<sup>38</sup> Various fabrication techniques have been investigated to pattern liquid metals into flexible electrodes, including direct writing,<sup>39</sup> selective plating,<sup>40,41</sup> stencil printing,<sup>42,43</sup> micro-channeling,<sup>44,45</sup> and mechanical sintering of liquid metal particles (LMPs).<sup>46,47</sup> However, these techniques typically require complicated processes, limiting the applications of liquid metal patterning on a flat surface. It still remains a challenge to create three-dimensional liquid metal electrodes on soft elastomers for device performance improvement.

Herein, we have developed an integrated and cost-effective capacitive sensor for ultraflexible and sensitive contact pressure sensing. This arrayed sensor is constructed on a liquid metal

film electrode featured with a three-dimensional icicle-shaped structure. Figure 1a,b shows the photograph and schematic illustration of a  $4 \times 4$  arrayed pressure sensor. The device consists of two stretchable elastomer layers encapsulated with liquid metal lines/films placed orthogonally to each other. The top electrode layer containing the icicle-shaped liquid metal film allows for an enhanced pressure perception. Specifically, an external pressure largely deforms the microstructure and, accordingly, results in the deformation of the embedded electrodes, leading to the changes in both overlapping area and separation distance. The unique icicle-shaped electrode/elastomer design enables the pressure detection as low as 12 Pa, with a high sensitivity of  $39\% \text{ kPa}^{-1}$  in the range of 0–1 kPa. The sensor exhibits a minimal hysteresis error of 8.46% ranging from 0 to 25 kPa. Our flexible pressure sensor array is accurate and robust even in a high stretching condition, by up to 94% strain (approximately the strain of human skin at joints<sup>48</sup>), without affecting its function. We have demonstrated an excellent reliability under various environmental conditions, including temperature (30–105 °C) and humidity (40–80% RH), and thousands of load/unload cycles. As proof-of-concept, our arrayed sensor has been successfully applied to force measurements on a curved surface, contour mapping of the external loads, and distinguishing the dynamic cervical postures.

## EXPERIMENTAL SECTION

**Materials.** Eutectic Ga–In (EGaIn) with the composition of 75% Ga and 25% In was purchased from Sigma-Aldrich. The elastomer (Ecoflex 00-30) was purchased from Smooth-On, Inc., and used as received. Corning 96-well TC-treated microplates with round wells of 360  $\mu\text{L}$  were purchased from Sigma-Aldrich.

**Fabrication of the Electrodes.** The fabrication process is illustrated in Figure 1e–j. Liquid Ecoflex 00-30 is prepared by mixing the components of part A and part B at a mass ratio of 1:1, followed

with sufficient stirring. The mixture is spun onto a silicon wafer pretreated with the releasing agent (surfactant) at 500 rpm for 10 s and 1000 rpm for 1 min. The wafer is then put into a vacuum chamber to remove the air bubbles in the Ecoflex layer. After the elastomer layer is fully cured at room temperature (Figure 1e,f), conductive cloth tapes (3MCEF series, 3M) are attached to the membrane for electrical connection between the liquid metal electrodes and wires (Figure 1g).

The electrode pattern is deposited on the Ecoflex membrane by atomized spraying of EGaIn through a customized stencil made of stainless steel (Figure 1h,i). EGaIn is filled into an airbrush and is sprayed through a nozzle for 5 s with constant compressed air produced by a pump. The air pressure is set to 40 psi. The distance between the nozzle and the stencil is 20 cm.

Before peeling from the wafer, 3 g of Ecoflex is mildly spun onto the electrode as an additional elastomeric support, which is cured at 60 °C for 10 min (Figure 1j). The flat EGaIn/Ecoflex composite electrode is then cleansed with ethanol after demolding, followed with drying.

**Construction of the Icicle-Shaped Liquid Metal Film Electrode.** A pair of electrodes are fabricated simultaneously through the process described above. One of the as-prepared electrodes is further processed for the icicle shape, assisted with a 96-well plate as the mold. There is a critical challenge for fabrication of a three-dimensional configuration, due to the fluidity of liquid metal. We develop a straightforward process to overcome the challenge, by taking advantage of the stretchability of both the liquid metal and Ecoflex. The liquid metal is pre-encapsulated in Ecoflex before modifying the configuration by applying a negative pressure. A 96-well plate is utilized as a mold to create the icicle shape for the electrode. The process is shown schematically in Figure 1k–p. An electrode is spread over the mold, with the side of dielectric elastomer membrane facing the mold, and the EGaIn stripes are aligned to the wells. The electrode is gently pressed against the mold to ensure good seal before the electrode is put into a vacuum chamber together with the mold. A negative pressure is applied for 30 s, lowering the pressure on both sides of the electrode (Figure 1l). Subsequently, gas flows into the vacuum chamber during ventilation, and a pressure difference appears above and below the electrode, which is contributed by the excellent sealing property of Ecoflex to maintain the vacuum between the membrane and the wells. It renders the electrode deformed toward the mold, becoming the icicle shape. Then, more Ecoflex is added and cured as the back support to consolidate the icicle-shaped deformation before peeling off (Figure 1m,n). The degree of deformation can be controlled by adjusting the value of negative pressure. The optimal value is  $-0.03$  MPa to achieve best sensitivity and stability. Afterward, more Ecoflex is applied and cured before peeling the electrode from the mold (Figure 1o,p), so that the icicle shape can be kept for the liquid metal film electrode after releasing.

**Assembly of the Arrayed Sensor.** Our primary sensor is finally assembled by two EGaIn/Ecoflex composites: one with an array of icicle-shaped liquid metal film electrodes and the other with a flat liquid metal film electrode (Figure 1b). The two electrodes are stacked perpendicularly, with the dielectric layers inward, and the bulges on the top layer are aligned right on the center of EGaIn stripes of the other electrode (the bottom layer). To fix the relative position of the two electrodes, tiny amount of Ecoflex is utilized to bond the bulges surrounding the sensing units to the other electrode.

**Characterization of Electrical and Mechanical Properties.** The capacitance is measured by an impedance analyzer (6500B, Wayne Kerr) with a driving frequency of 15 kHz after optimization to ensure stable capacitance outputs (Figure S1). A force gauge with 0.5 mN resolution (MS-05, Mark-10, Corp.) is connected with a step motor (LTS300/M, Thorlabs, Inc.), which can be programmed to move with a resolution of  $0.1 \mu\text{m}$ . These devices are connected to a computer, which controls the movement of the step motor and collects the data of capacitance and force. Our data typically sample 50 independent readouts to calculate the mean values and standard deviations. Ambient temperature and humidity are adjusted by a hot plate and a humidifier, respectively. For the application of detecting

cervical postures, the sensor array is attached to the cervical region of a volunteer and is fixed by an adhesive tape, and the capacitance outputs are recorded as the volunteer performs different cervical postures.

**Numerical Simulations.** COMSOL simulations are conducted to analyze the mechanical deformation of the icicle-shaped elastomer under mechanical loads. To simplify the sensor model, only the Ecoflex elastomer parts are built, with a pre-assumption that the modulus of the liquid metal material is negligible. Similar to the sensor structure, the overall numerical model consists of a layer of icicle-shaped Ecoflex elastomer and a flat Ecoflex membrane. The radius of the curvature and the height for elastomer bump are 3.5 and 3.08 mm, respectively. Young's modulus and Poisson's ratio are 120 kPa and 0.495, respectively. The icicle-shaped layer is set to be stationary. The physical parameters, such as the stress and strain on the icicle-shaped Ecoflex, are recorded. When an initial displacement is applied on the flat membrane, both the bump and the flat membrane may take place of mechanical deformations.

## RESULTS AND DISCUSSION

**Sensor Structure and Working Principle for Flexible Force Measurements.** The sensor comprises arrayed capacitors, which are constructed by top and bottom liquid metal film electrodes embedded in a dielectric Ecoflex elastomer. The top electrode layer consists of an array of icicle-shaped EGaIn/Ecoflex composites. The bottom electrode layer is constructed on a flat EGaIn/Ecoflex substrate. Each of the electrode lines/films is completely covered by a thin dielectric Ecoflex membrane for electrical insulation. The two electrode layers are stacked perpendicularly with the thin dielectric Ecoflex membrane sandwiched in between. Figure 1c is the cross-sectional illustration of a single sensing unit without external stimuli. The top liquid metal electrode winds along the Ecoflex bump, initiating the maximum separation distance and the minimum overlapping area at the zero-force state. As shown in Figure 1d, the external load can compress the bulge of the icicle-shaped liquid metal film electrode, leading to an increase of the effective overlapping area and a decrease of the separation distance of the capacitor. The overall capacitance  $C$  can be predicted by the classic equation of the parallel-plate capacitor:  $C = \frac{\epsilon_0 \epsilon_r A}{d}$ , where  $\epsilon_0$  is the absolute dielectric constant,  $\epsilon_r$  is the relative permittivity of the material between the electrodes, and  $A$  and  $d$  represent the effective overlapping area and separation distance of the electrodes, respectively.

**Experimental Optimization and Performance Characterization.** We have performed experiments to reveal the relationship between the geometrical features of the icicle-shaped liquid metal film electrode (the top layer) and the negative pressures during fabrication. As shown in Figure S2a, the base length and the apex height of the bump structure of the electrode are defined as  $a$  and  $b$ , respectively. The dimensional feature ratio of  $b/a$ , indicating the deformation degree of the bump, can be adjusted by appropriately controlling the negative pressures on the film electrode. We have applied four different negative pressures, including 0,  $-0.02$ ,  $-0.03$ , and  $-0.04$  MPa, during the fabrication procedure, thus generating a series of icicle-shaped electrodes with the four  $b/a$  ratios (0, 0.23, 0.44, and 0.53, accordingly, as shown in Figure S2). Subsequently, five pilot sensors are designed by assembling the top and bottom layers (Figure S3) with various  $b/a$  ratios, including 0.53–0.53, 0.53–0, 0.44–0, 0.23–0, and 0–0, to investigate the structure–property relationship. The sensors with higher  $b/a$  ratios exhibit

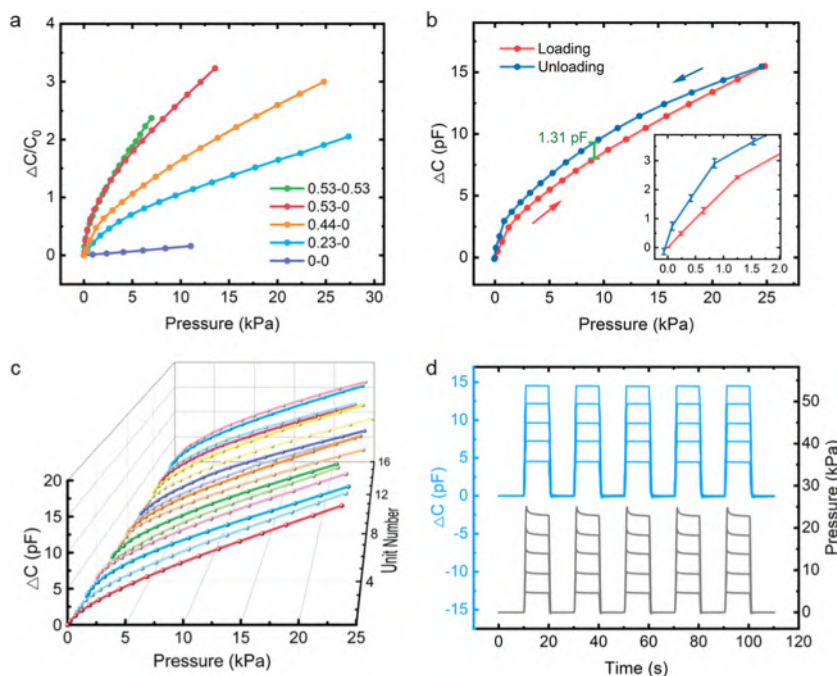


**Figure 2.** Capacitance-to-pressure responses of the sensor. (a) Electrical responses to the mechanical loads on five individual sensors with different electrode combinations (deformation degree of top–bottom electrodes: 0.53–0.53, 0.53–0, 0.44–0, 0.23–0, and 0–0). (b) Complete capacitance increment–pressure curve of a sensing unit in the mechanical loading/releasing cycle in the range of 0–25 kPa. The maximum difference between the loading and unloading curves: 1.31 pF. Inset: a zoomed-in view of the range (0–2 kPa). (c) Capacitance increment–pressure curves of 16 units in a sensor array (4 × 4), showing a high consistency among the individual units. (d) Time-resolved pressure curves (gray lines) and the corresponding capacitance readout curves (blue lines) in a periodic loading/releasing pattern (in the range of 4.5–22.8 kPa, 5 cycles, 1 sensing unit).

relatively smaller initial capacitance values (Figure S4). The relative capacitance changes ( $\Delta C/C_0$ ) of those sensors in response to the external mechanical loads are compared in Figure 2a. The sensor with top and bottom flat electrodes (noted as 0–0) shows a minimum capacitive change ( $\Delta C < 3$  pF) in the pressure range of 0–10 kPa compared with the other types of sensors. As the  $b/a$  ratio in the top electrode layer increases, i.e., 0.23–0, 0.44–0, and 0.53–0, the capacitive outputs increase by 1.7, 2.0, and 2.4 times compared to the one with flat electrodes. It is clear that the bump structure facilitates the mechanical deformation of the electrode/elastomer, leading to a significant increase in the overlapping area as well as a decrease of the distance between the electrodes. Both factors can enhance the capacitance output in the force measurements. In addition, the capacitance output rises as the deformation degree of bump structure ( $b/a$  ratio) increases, also due to magnification by these two factors above. The sensor with both top and bottom icicle-shaped electrodes (0.53–0.53) shows a similar electrical response to the sensor with a simplified geometry, that is, one icicle-shaped electrode assembled on a flat electrode (0.53–0), in the range of 0–4 kPa. After balancing the initial capacitance, sensitivity, and the flexibility of the whole device, we have chosen the sensor built on a top electrode of  $b/a = 0.44$  and a flat bottom electrode (0.44–0) as the optimal device for the subsequent tests. The effect on the pressure sensing by the changes in the dielectric layer thickness has been investigated, which suggests an inverse correlation between the initial capacitance ( $C_0$ ) values (6.16, 5.17, and 4.55 pF, respectively) and the parameters of thickness (73, 85, and 106  $\mu\text{m}$ ). The sensitivity difference of those sensors ( $\Delta C/C_0$ ) is relatively small in the thickness range of our tests (Figure S5).

Figure 2b shows the capacitance variations in response to a pressure increasing from 0 to 25 kPa and then decreasing backward to 0. The device sensitivity is defined as

$$S = \frac{d\left(\frac{C-C_0}{C_0}\right)}{dP}$$

As shown in the inset in Figure 2b, the sensor features a higher sensitivity ( $S = 39\% \text{ kPa}^{-1}$ ) in the small pressure range (0–1 kPa). The sensitivity drops to  $15\% \text{ kPa}^{-1}$  in the range of 1–6 kPa (approximately the pressure generated by a gentle touch<sup>49</sup>) and  $10\% \text{ kPa}^{-1}$  in the range of 6–25 kPa, which is in good agreement with the simulation results (Figure S6). In addition, we have analyzed the device hysteresis error, which is calculated by the ratio of the maximum difference between the loading and unloading curves ( $\Delta H_{\text{max}}$ ) to the full-scale output reading ( $y_{\text{FS}}$ ). Hysteresis error:

$$\delta_H = \frac{\Delta H_{\text{max}}}{y_{\text{FS}}} \times 100\%$$

In this work, the hysteresis error is estimated as 8.46% in the pressure range of 0–25 kPa. The hysteresis value is slightly higher than that for the sensors with microstructured sensing elements,<sup>11,13,50</sup> which is possibly derived from the intrinsic viscoelasticity difference of the elastomer as well as the weak adhesion between the dielectric Ecoflex membrane and the liquid metal electrode.<sup>10</sup> The capacitance change of the sensor is recorded under the extreme pressure available by our instrumental setup. As shown in Figure S7, the capacitance reaches the maximum (26.4 pF) when the external pressure increases to 37 kPa and keeps at the plateau value due to no room for any new change in the electrode area or distance when the pressure exceeds 37 kPa (up to 120 kPa). The capacitance can recover to the initial value once the external pressure is released, indicating an outstanding robustness for the sensors to endure high mechanical loads. We have examined the consistency in the

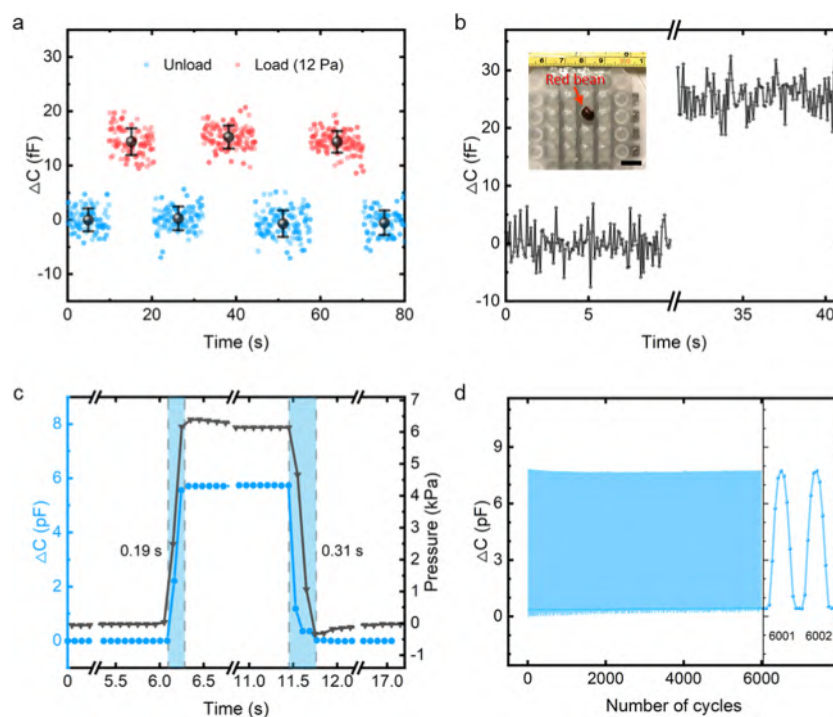


**Figure 3.** Limit of detection, response time, and reliability evaluation. (a) Limit of detection of a sensing unit in a periodic pattern of load/unload (12 Pa; blue dots: unload, red dots: load, dark dots, mean values). Sampling frequency: 12.5 Hz. (b) Capacitance increments of a sensing unit before and after placing a plant seed (a red bean,  $\sim 0.2$  g). Inset: a photo of the test. Scale bar: 1 cm. (c) Capacitance changes in real time with the mechanical load/unload ( $\sim 6$  kPa), suggesting a good synchronism. (d) Dot-line plot of capacitance changes against 6000 load/unload cycles, indicating a robust and reproducible performance of the sensor. Mechanical load/unload frequency: 0.5 Hz. Capacitance sampling frequency: 6 Hz.

mechanical–electrical property for all of the 16 sensing units in a  $4 \times 4$  array. In Figure 2c, the capacitance change–pressure curves of the 16 individual units are presented according to the number of their spatial locations. All of the curves show a similar increment in the pressure range of 0–25 kPa, with a minimal variation of  $0.48\% \text{ kPa}^{-1}$  in device sensitivity. This suggests a highly reproducible performance among each individual sensing unit, thus promising accurate pressure distribution measurements in a standard calibration procedure.

Furthermore, the repeatability of our sensor under a dynamic load has been examined. Periodic loads with five different pressure values at a frequency of 0.05 Hz are applied on one sensing unit in the sensor array. The capacitance outputs are recorded at a sampling frequency of 12.5 Hz. Figure 2d plots the time-resolved capacitance (blue lines) and pressure (gray lines) changes. As the pressure varies from 4.5 to 9.0, 13.8, 18.2, and 22.8 kPa, the corresponding capacitance increases from 4.54 to 7.25, 9.64, 12.18, and 14.55 pF. Therefore, repeatable signal readout has been validated for the sensor with the characteristic profiles of capacitances to dynamic loads in all of the cycles.

The data in Figure 3a reveal the limit of detection (LOD) of the sensor in the force measurements. Under a periodic load (1 mN force, corresponding to 12 Pa), the capacitance outputs have been recorded in real time with a sampling frequency of 12.5 Hz. The capacitance readouts with or without the load are represented by the scattered red or blue dots, while the mean capacitive values by the black dots. The capacitance increment of 15 fF can be easily distinguished from the noise level ( $\sim 6.33$  fF), indicating the LOD ( $\leq 12$  Pa) for our sensor. Figure 3b demonstrates that our sensor sensitively detects the weight of a

tiny red bean ( $\sim 0.2$  g) with a capacitance change of about 25 fF.

We have further investigated the response/recovery time of the sensor (Figure 3c). An external load (6 kPa) is applied on the sensor for 5 s and then released. The capacitance (blue dotted line) and pressure (gray dotted line) are recorded with sampling frequencies of 12.5 and 10 Hz, respectively. As shown in Figure 3c, the capacitance changes are highly synchronized with the pressures. Based on the ramp details in the curves, it takes 0.19 s for the sensor to respond to the external pressure, during which the capacitance is promoted to a plateau value of 5.7 pF. Reversely, the recovery time is estimated as 0.31 s for the sensor after removal of the pressure.

The mechanical reliability and robustness of our sensor have been evaluated by testing the sensor with thousands of press-and-release cycles at a frequency of 0.5 Hz using a step motor. As shown in Figure 3d, the sensor maintains a very stable output of the electrical signals under the periodic load of about 8 kPa. The peak value is shifted by only  $-1.3\%$  after 6000 cycles. This demonstrates an ultrarobust performance of our device in the mechanical properties and electrical reliability.

#### Reliability in Different Force Measurement Scenarios.

In the field of developing flexible contact force/pressure sensors, there are specific requirements on the flexibility and stretchability. These properties are important to help the sensors comply with complicated structures or surfaces for sufficient accuracy during the measurements. Here, we have investigated the electrical responses when our sensor is in a bending or stretching state. As illustrated in Figure 4a, the arrayed sensor is wrapped on a surface of a 50 mL centrifuge tube. The radius of curvature defined by the tube is estimated as 15 mm. The sensor is pressed by the force gauge with a

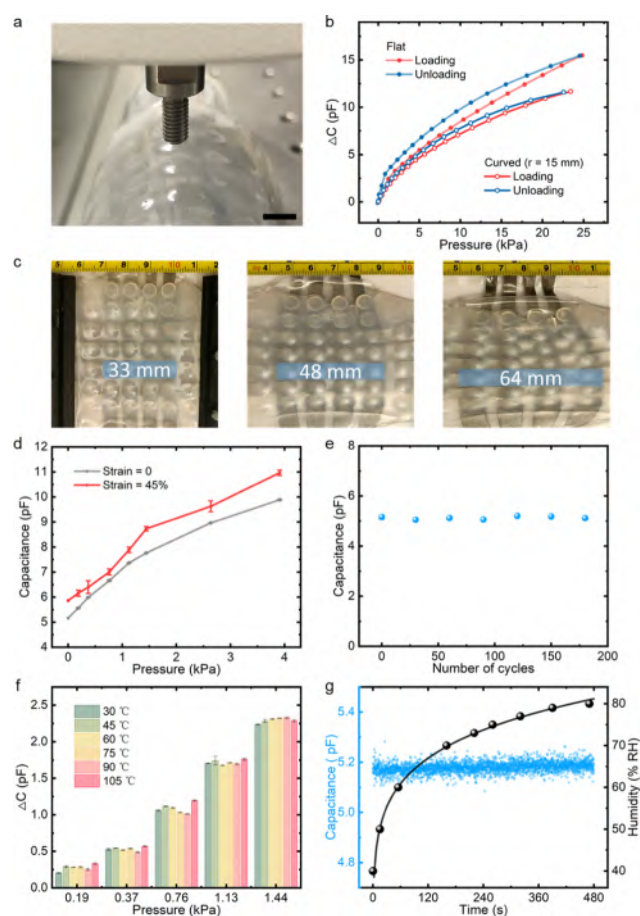


**Figure 4.** Force measurements on the curved surface and the robust performance immune to the environmental temperature/humidity variations. (a) Photograph of bending the sensor arrays along a 50 mL centrifuge tube as the test setup. Radius of the tube: 15 mm. Scale bar: 5 mm. (b) Comparison of the capacitance change–pressure curves in the bending and unbending states. (c) Photographs of the sensor array at different stretching extents of 0, 45, and 94% strain. (d) Capacitance responses to an additional mechanical load (0–4 kPa) at 0 strain (gray line) and 45% strain (red line). Error bar: standard deviation ( $n = 3$ ). (e) Back-to-default capacitance of a sensor unit after periodic stretching/releasing (at 94% strain, 180 cycles, 1 capacitive readout every 30 cycles). (f) Capacitance change–pressure relationship at different temperatures (30–105 °C), suggesting a robust performance immune to the environmental temperature changes. Error bar: standard deviation ( $n = 3$ ). (g) Capacitance of a sensing unit measured in an ambient humidity from 40 to 80% RH (blue dots: capacitance, black dots: humidity), suggesting a robust performance immune to the environmental humidity changes.

constant step distance of 200  $\mu\text{m}$  and then released to the original position. The capacitance changes of the sensor along with the applied pressures are compared in combinatorial scenarios of the curved/flat surface and mechanical loading/unloading (Figure 4b). The overall capacitance increment of the sensor on the curved surface is reduced by nearly 20% in comparison to that on the flat surface. The hysteresis error of the curved sensor (5.19%) is smaller compared to that of the flat one (8.46%). This indicates that the icicle-shaped electrode may be slightly compressed in the bending state, leading to a decreased sensitivity. However, the defects, such as air gaps during the sensor assembly, could be amended as the sensor gets bended, thus mitigating the load/unload hysteresis.

Besides the bending, the influence of mechanical stretch on the sensor performance has been tested by our experiments. Although a lot of flexible sensors have been reported in the literature, many of them suffer from poor stretchability and compromised performance under mechanical stretching. Here, in our work, photographs in Figure 4c show the arrayed sensor in different stretching states with a strain of 0, 45, and 94%. No obvious crack in the electrodes or elastomer is observed in the process of stretching, thanks to the fluidity of liquid metal and the superb elasticity of Ecoflex. Figure 4d summarizes the mechanical–electrical performance of our sensor in both normal (0% strain) and stretched (45% strain) states. Identical mechanical loads in the range of 0–4 kPa are applied to the same sensing unit. In the stretched state, the initial capacitance increases by 0.69 pF, while the slopes of the curves show little difference between the two states, indicating a reliable performance under the stretching condition. The reliability is primarily contributed by the unique structure of our sensor. To be specific, each sensing unit consists of a bulging bump and the surrounding flat membrane. The most of the strain tends to be distributed on the flat membrane section rather than the bulging structure, resulting in a negligible change in the capacitance under a mechanical strain, as revealed by the simulations in Figure S8. The initial capacitance values are recorded when the sensor is stretched to a strain of 94% and released to the normal state for 180 cycles (Figure 4e). The coefficient of variation (CV) value is smaller than 1.2%, indicating that our sensor endures the repeated large mechanical stretching very well. The maximal stretchability is determined to withstand up to 173% strain without damage (Figure S9).

We have also investigated the environmental influences, including temperature or humidity, on our sensor. Figure 4f shows the capacitance responses to five different mechanical loads under temperatures ranging from 30 to 105 °C. The capacitance increment–pressure curves only present negligible difference at different temperatures. The time-resolved capacitance output is recorded at the sampling frequency of 5.5 Hz, when the environmental humidity gradually rises from room condition (40% RH) to an elevated level (80% RH). As shown in Figure 4g, there is a stable performance for our sensor to produce the signal readout, independent of the humidity variations. The CV value of the outputs is 0.6%.

**Potential Applications of the Arrayed Sensor.** To demonstrate two-dimensional pressure distribution measurements to distinguish external loading sources, we have tested our 4  $\times$  4 arrayed sensor using two different types of loads (Figure 5a–f). They include a solid cylinder (20 g, 13 mm in diameter, Figure 5a) and a ring-shaped tape (16 g, 52 mm in diameter, Figure 5d). The pressures in each sensing unit (Figure 5b,e) are calculated from the corresponding unit capacitance changes by reference to the capacitance change–pressure calibration curves (Figure 2c). As the weight with a small contact area stands on the sensing device, unit #7 (as marked in Figure 5a) takes the most of the load of 1.41 kPa. Adjacent units have a little pressure increments by 0.45 kPa (unit #3), 0.18 kPa (unit #8), 0.10 kPa (unit #6), 0.08 kPa (unit #11), and 0.04 kPa (unit #4). In comparison, the tape generates a distinct pattern for the pressure distribution when it is loaded onto our sensor. As predicted, the sensing units in the corner positions of the arrays take the most of the load (0.16–0.21 kPa), followed by the units on the four edges (0.07–0.13 kPa). Figure 5c,f presents the contour plots of the

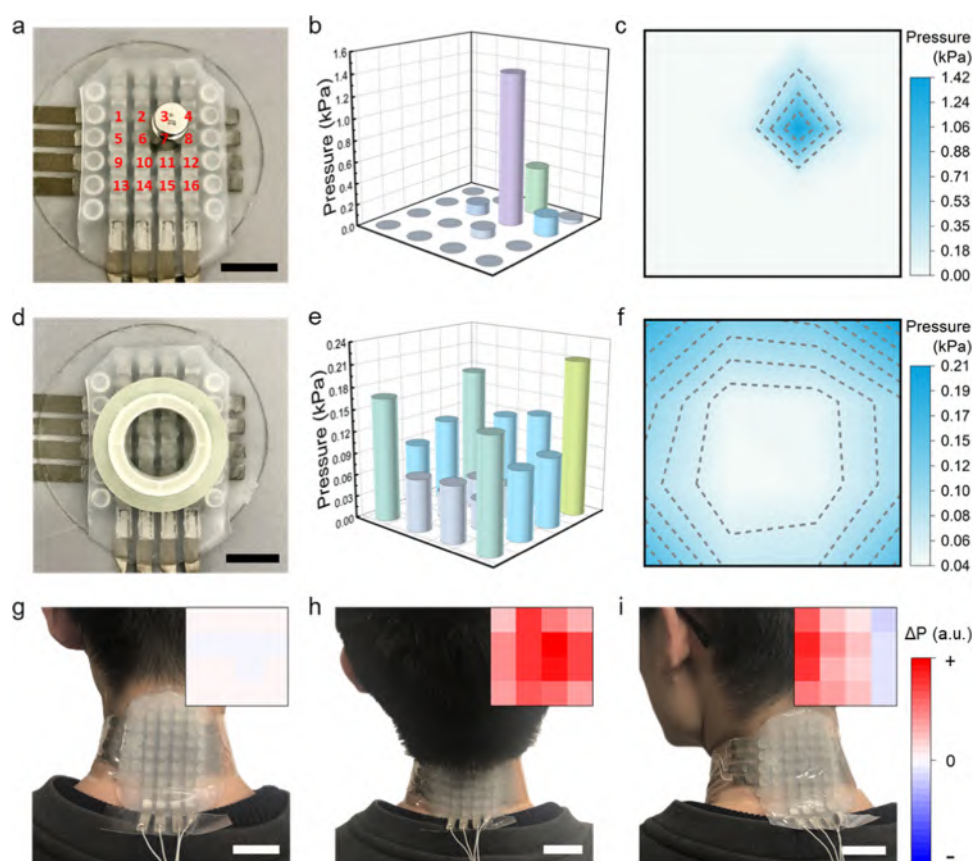


**Figure 5.** Device applications. (a) Photograph showing the top view of a standard weight (20 g) on the  $4 \times 4$  sensor array. The sensing units are labeled from #1 to #16. The weight is placed approximately on unit #7. Scale bar: 2 cm. (b, c) Three-dimensional bar graph and a contour plot of the pressure distribution on the sensor arrays. (d) Photograph showing the top view of a ring-shaped tape (about 16 g) on the sensor arrays. Scale bar: 2 cm. The diameter of the tape is slightly larger than the sensor array. (e, f) Three-dimensional bar graph and a contour plot of pressure distribution by the tape on the sensor array. (g) Photograph showing the sensor array attached on the cervical region of the volunteer. Head posture: looking straight ahead. Scale bar: 3 cm. Inset: Heat map of the pressures on each sensing unit in this posture defined as the default values ( $\Delta P = 0$ ). (h, i) Cervical posture of raising the head up or rotating the head toward the left. Scale bar: 3 cm. Insets: Heat maps of the pressure changes on the sensor arrays relative to the default. Red: increasing. Blue: decreasing.

pressures in these two cases, clearly mapping both the load positions and the intensities characteristic to the external loading sources.

In the experiments, to evaluate the potential crosstalk between the units, the capacitance changes of the sensor arrays are monitored while the mechanical load (8 kPa) is applied onto the individual units one-by-one (the unit #6, unit #7, unit #10, and unit #11). We choose a small force gauge tip (3 mm in diameter) to ensure the physical contact onto the individual testing unit. As shown in Figure S10, the capacitance change on the testing units is measured as  $7.39 \pm 0.14$  pF, while the capacitance changes of neighboring units are below 0.44 pF. This indicates a high ratio of the signal to the crosstalk.

With the changes of people's living and working styles, excessive use of computers and mobile phones puts great pressure on people's cervical vertebrae, which led to the increasing prevalence of cervical spondylosis in recent years. Bad postures in sleeping, working, and physical exercise can cause chronic strain in the cervical region. If not taken seriously, cervical spondylosis could even get worse, and vertebral artery oppression could develop dizziness and nausea.<sup>51</sup> Therefore, monitoring cervical postures by wearable electronic sensors is of great interest for the prevention of cervical spondylosis. We have demonstrated monitoring the contact pressures between our sensor and the cervical region

for identification of cervical postures. Our arrayed sensor is elastic and flexible to ensure a good fit while wearing on neck and accommodate the measurements of cervical movements. It is attached to the skin with assistance of an adhesive tape. The default load is defined as the contact pressure of the sensor with the neck as the volunteer looks straight ahead, as illustrated in Figure 5g. The capacitance of each sensing unit is set as the default value at this posture. The capacitance changes are calculated while the volunteer is performing various cervical postures. Figure 5h illustrates a posture of heading up, with the pressure changes displayed in the inset. Each of the sensing unit turns red, indicating an increased pressure compared with the defaults at the looking-straight posture. Importantly, the units in the center show larger pressure increments than the units at the corners, suggesting that the spinous process of cervical vertebra is subjected to most of the stress. When the volunteer rotates the head to the left, a gradient of pressure increment appears across the columns (Figure 5i). The sensing units in the left edge show larger pressure increments, while the units in the right edge show decreases in pressure (shown in the blue color), suggesting that the stress is mainly concentrated in the side the head is rotated toward. By analyzing the pressure distribution of the cervical region, different cervical postures can be identified, which promise consequent references for real-time cervical

posture analysis. The arrayed sensor can be applied for detection of unhealthy cervical postures of the patients undergoing rehabilitation trainings by providing a timely reminder.

## CONCLUSIONS

In summary, we have developed a new method to fabricate the highly stretchable capacitive pressure sensor array featuring with icicle-shaped liquid metal film electrodes. This method is straightforward and cost-effective, and there is no need for complicated MEMS processes or additional packaging. Our sensor exhibits a high sensitivity of 39% kPa<sup>-1</sup> in the region of gentle pressures (0–1 kPa), while maintaining an outstanding stretchability. The capacitance-to-pressure sensitivity is immune to stretching, with a robust performance even after being stretched to 94% strain for 180 cycles. Our arrayed sensor has been successfully utilized to map surface pressure distributions, including the contact pressure measurements for head/cervical posture analysis for rehabilitation guidance. This unique pressure sensing solution promises a wide range of emerging applications as an active module of wearable electronics.

## ASSOCIATED CONTENT

### Supporting Information

The Supporting Information is available free of charge at <https://pubs.acs.org/doi/10.1021/acsami.0c04939>.

Tests of sweeping frequency; the relationship between the dimensional feature ratio ( $b/a$ ) and the negative pressures during fabrication; cross-sectional view of a sensing unit; initial capacitance of the sensors with different feature ratios; effect of dielectric layer thickness; mechanical breakdown limit of pressure/stretchability; simulations; and crosstalk evaluation of individual units (PDF)

## AUTHOR INFORMATION

### Corresponding Authors

**Baoqing Nie** – School of Electronic and Information Engineering, Soochow University, Suzhou, Jiangsu 215006, China; Email: [qixinbq@suda.edu.cn](mailto:qixinbq@suda.edu.cn)

**Jian Liu** – Institute of Functional Nano and Soft Materials (FUNSOM), Jiangsu Key Laboratory for Carbon-Based Functional Materials and Devices, Soochow University, Suzhou, Jiangsu 215123, China; [orcid.org/0000-0002-0095-8978](https://orcid.org/0000-0002-0095-8978); Email: [jliu@suda.edu.cn](mailto:jliu@suda.edu.cn)

### Authors

**Yiqiu Zhang** – Institute of Functional Nano and Soft Materials (FUNSOM), Jiangsu Key Laboratory for Carbon-Based Functional Materials and Devices, Soochow University, Suzhou, Jiangsu 215123, China; [orcid.org/0000-0002-0206-0061](https://orcid.org/0000-0002-0206-0061)

**Sidi Liu** – Institute of Functional Nano and Soft Materials (FUNSOM), Jiangsu Key Laboratory for Carbon-Based Functional Materials and Devices, Soochow University, Suzhou, Jiangsu 215123, China

**Yihui Miao** – School of Electronic and Information Engineering, Soochow University, Suzhou, Jiangsu 215006, China

**Han Yang** – School of Electronic and Information Engineering, Soochow University, Suzhou, Jiangsu 215006, China

**Xuyue Chen** – Institute of Functional Nano and Soft Materials (FUNSOM), Jiangsu Key Laboratory for Carbon-Based

Functional Materials and Devices, Soochow University, Suzhou, Jiangsu 215123, China

**Xiang Xiao** – Institute of Functional Nano and Soft Materials (FUNSOM), Jiangsu Key Laboratory for Carbon-Based Functional Materials and Devices, Soochow University, Suzhou, Jiangsu 215123, China

**Zhongyun Jiang** – Institute of Functional Nano and Soft Materials (FUNSOM), Jiangsu Key Laboratory for Carbon-Based Functional Materials and Devices, Soochow University, Suzhou, Jiangsu 215123, China

**Xinjian Chen** – School of Electronic and Information Engineering and State Key Laboratory of Radiation Medicine and Protection, Soochow University, Suzhou, Jiangsu 215006, China

Complete contact information is available at:

<https://pubs.acs.org/doi/10.1021/acsami.0c04939>

## Notes

The authors declare no competing financial interest.

## ACKNOWLEDGMENTS

This work is supported by the National Key Research and Development Program of China (2017YFE0131700) and the National Natural Science Foundation of China (21874096, 61601317, 21575095); a project supported by Collaborative Innovation Center of Suzhou Nano Science and Technology, the 111 Project, Joint International Research Laboratory of Carbon-Based Functional Materials and Devices, and the Priority Academic Program Development of Jiangsu Higher Education Institutions (PAPD).

## REFERENCES

- (1) Li, X.; Li, M.; Xu, J.; You, J.; Yang, Z.; Li, C. Evaporation-Induced Sintering of Liquid Metal Droplets with Biological Nanofibrils for Flexible Conductivity and Responsive Actuation. *Nat. Commun.* **2019**, *10*, No. 3514.
- (2) Pan, L.; Chortos, A.; Yu, G.; Wang, Y.; Isaacson, S.; Allen, R.; Shi, Y.; Dauskardt, R.; Bao, Z. An Ultra-Sensitive Resistive Pressure Sensor Based on Hollow-Sphere Microstructure Induced Elasticity in Conducting Polymer Film. *Nat. Commun.* **2014**, *5*, No. 3002.
- (3) Nie, B.; Huang, R.; Yao, T.; Zhang, Y.; Miao, Y.; Liu, C.; Liu, J.; Chen, X. Textile-Based Wireless Pressure Sensor Array for Human-Interactive Sensing. *Adv. Funct. Mater.* **2019**, *29*, No. 1808786.
- (4) Zou, B.; Chen, Y.; Liu, Y.; Xie, R.; Du, Q.; Zhang, T.; Shen, Y.; Zheng, B.; Li, S.; Wu, J.; Zhang, W.; Huang, W.; Huang, X.; Huo, F. Repurposed Leather with Sensing Capabilities for Multifunctional Electronic Skin. *Adv. Sci.* **2019**, *6*, No. 1801283.
- (5) Won, D.-J.; Baek, S.; Huh, M.; Kim, H.; Lee, S.; Kim, J. Robust Capacitive Touch Sensor Using Liquid Metal Droplets with Large Dynamic Range. *Sens. Actuators, A* **2017**, *259*, 105–111.
- (6) Gu, Y.; Zhang, T.; Chen, H.; Wang, F.; Pu, Y.; Gao, C.; Li, S. Mini Review on Flexible and Wearable Electronics for Monitoring Human Health Information. *Nanoscale Res. Lett.* **2019**, *14*, No. 263.
- (7) Nie, B.; Yao, T.; Zhang, Y.; Liu, J.; Chen, X. A Droplet-Based Passive Force Sensor for Remote Tactile Sensing Applications. *Appl. Phys. Lett.* **2018**, *112*, No. 031904.
- (8) Reynolds, V. G.; Mukherjee, S.; Xie, R.; Levi, A. E.; Atassi, A.; Uchiyama, T.; Wang, H.; Chabinye, M. L.; Bates, C. M. Super-Soft Solvent-Free Bottlebrush Elastomers for Touch Sensing. *Mater. Horiz.* **2020**, *7*, 181–187.
- (9) Wang, X.; Liu, Z.; Zhang, T. Flexible Sensing Electronics for Wearable/Attachable Health Monitoring. *Small* **2017**, *13*, No. 1602790.
- (10) Yang, J. C.; Mun, J.; Kwon, S. Y.; Park, S.; Bao, Z.; Park, S. Electronic Skin: Recent Progress and Future Prospects for Skin-

Attachable Devices for Health Monitoring, Robotics, and Prosthetics. *Adv. Mater.* **2019**, *31*, No. 1904765.

(11) Mannsfeld, S. C.; Tee, B. C.; Stoltenberg, R. M.; Chen, C. V.; Barman, S.; Muir, B. V.; Sokolov, A. N.; Reese, C.; Bao, Z. Highly Sensitive Flexible Pressure Sensors with Microstructured Rubber Dielectric Layers. *Nat. Mater.* **2010**, *9*, 859–864.

(12) He, K.; Hou, Y.; Yi, C.; Li, N.; Sui, F.; Yang, B.; Gu, G.; Li, W.; Wang, Z.; Li, Y.; Tao, G.; Wei, L.; Yang, C.; Chen, M. High-Performance Zero-Standby-Power-Consumption-under-Bending Pressure Sensors for Artificial Reflex Arc. *Nano Energy* **2020**, *73*, No. 104743.

(13) Cho, S. H.; Lee, S. W.; Yu, S.; Kim, H.; Chang, S.; Kang, D.; Hwang, I.; Kang, H. S.; Jeong, B.; Kim, E. H.; Cho, S. M.; Kim, K. L.; Lee, H.; Shim, W.; Park, C. Micropatterned Pyramidal Ionic Gels for Sensing Broad-Range Pressures with High Sensitivity. *ACS Appl. Mater. Interfaces* **2017**, *9*, 10128–10135.

(14) Kim, H.; Kim, G.; Kim, T.; Lee, S.; Kang, D.; Hwang, M. S.; Chae, Y.; Kang, S.; Lee, H.; Park, H. G.; Shim, W. Transparent, Flexible, Conformal Capacitive Pressure Sensors with Nanoparticles. *Small* **2018**, *14*, No. 1703432.

(15) Chen, M.; Xia, J.; Zhou, J.; Zeng, Q.; Li, K.; Fujisawa, K.; Fu, W.; Zhang, T.; Zhang, J.; Wang, Z.; Wang, Z.; Jia, X.; Terrones, M.; Shen, Z. X.; Liu, Z.; Wei, L. Ordered and Atomically Perfect Fragmentation of Layered Transition Metal Dichalcogenides via Mechanical Instabilities. *ACS Nano* **2017**, *11*, 9191–9199.

(16) Chen, M.; Wang, Z.; Ge, X.; Wang, Z.; Fujisawa, K.; Xia, J.; Zeng, Q.; Li, K.; Zhang, T.; Zhang, Q.; Chen, M.; Zhang, N.; Wu, T.; Ma, S.; Gu, G.; Shen, Z.; Liu, L.; Liu, Z.; Terrones, M.; Wei, L. Controlled Fragmentation of Single-Atom-Thick Polycrystalline Graphene. *Matter* **2020**, *2*, 666–679.

(17) Chen, M.; Li, K.; Cheng, G.; He, K.; Li, W.; Zhang, D.; Li, W.; Feng, Y.; Wei, L.; Li, W.; Zhong, G. H.; Yang, C. Touchpoint-Tailored Ultrasensitive Piezoresistive Pressure Sensors with a Broad Dynamic Response Range and Low Detection Limit. *ACS Appl. Mater. Interfaces* **2019**, *11*, 2551–2558.

(18) Kim, H.; Lee, S. W.; Joh, H.; Seong, M.; Lee, W. S.; Kang, M. S.; Pyo, J. B.; Oh, S. J. Chemically Designed Metallic/Insulating Hybrid Nanostructures with Silver Nanocrystals for Highly Sensitive Wearable Pressure Sensors. *ACS Appl. Mater. Interfaces* **2018**, *10*, 1389–1398.

(19) Atalay, O.; Atalay, A.; Gafford, J.; Walsh, C. A Highly Sensitive Capacitive-Based Soft Pressure Sensor Based on a Conductive Fabric and a Microporous Dielectric Layer. *Adv. Mater. Technol.* **2018**, *3*, No. 1700237.

(20) Pruvost, M.; Smit, W. J.; Monteux, C.; Poulin, P.; Colin, A. Polymeric Foams for Flexible and Highly Sensitive Low-Pressure Capacitive Sensors. *npj Flexible Electron.* **2019**, *3*, No. 7.

(21) Wang, Z.; Jiang, R.; Li, G.; Chen, Y.; Tang, Z.; Wang, Y.; Liu, Z.; Jiang, H.; Zhi, C. Flexible Dual-Mode Tactile Sensor Derived from Three-Dimensional Porous Carbon Architecture. *ACS Appl. Mater. Interfaces* **2017**, *9*, 22685–22693.

(22) Kwon, D.; Lee, T. I.; Shim, J.; Ryu, S.; Kim, M. S.; Kim, S.; Kim, T. S.; Park, I. Highly Sensitive, Flexible, and Wearable Pressure Sensor Based on a Giant Piezocapacitive Effect of Three-Dimensional Microporous Elastomeric Dielectric Layer. *ACS Appl. Mater. Interfaces* **2016**, *8*, 16922–16931.

(23) Kim, S. J.; Mondal, S.; Min, B. K.; Choi, C. G. Highly Sensitive and Flexible Strain-Pressure Sensors with Cracked Paddy-Shaped MoS<sub>2</sub>/Graphene Foam/Ecoflex Hybrid Nanostructures. *ACS Appl. Mater. Interfaces* **2018**, *10*, 36377–36384.

(24) Chen, X.; Liu, H.; Zheng, Y.; Zhai, Y.; Liu, X.; Liu, C.; Mi, L.; Guo, Z.; Shen, C. Highly Compressible and Robust Polyimide/Carbon Nanotube Composite Aerogel for High-Performance Wearable Pressure Sensor. *ACS Appl. Mater. Interfaces* **2019**, *11*, 42594–42606.

(25) Xu, K.; Lu, Y.; Takei, K. Multifunctional Skin-Inspired Flexible Sensor Systems for Wearable Electronics. *Adv. Mater. Technol.* **2019**, *4*, No. 1800628.

(26) Zhao, X.; Hua, Q.; Yu, R.; Zhang, Y.; Pan, C. Flexible, Stretchable and Wearable Multifunctional Sensor Array as Artificial Electronic Skin for Static and Dynamic Strain Mapping. *Adv. Electron. Mater.* **2015**, *1*, No. 1500142.

(27) Han, L.; Lu, X.; Wang, M.; Gan, D.; Deng, W.; Wang, K.; Fang, L.; Liu, K.; Chan, C. W.; Tang, Y.; Weng, L. T.; Yuan, H. A Mussel-Inspired Conductive, Self-Adhesive, and Self-Healable Tough Hydrogel as Cell Stimulators and Implantable Bioelectronics. *Small* **2017**, *13*, No. 1601916.

(28) Cai, G.; Wang, J.; Qian, K.; Chen, J.; Li, S.; Lee, P. S. Extremely Stretchable Strain Sensors Based on Conductive Self-Healing Dynamic Cross-Links Hydrogels for Human-Motion Detection. *Adv. Sci.* **2017**, *4*, No. 1600190.

(29) Xiong, Y.; Shen, Y.; Tian, L.; Hu, Y.; Zhu, P.; Sun, R.; Wong, C.-P. A Flexible, Ultra-Highly Sensitive and Stable Capacitive Pressure Sensor with Convex Microarrays for Motion and Health Monitoring. *Nano Energy* **2020**, No. 104436.

(30) Boutry, C. M.; Negre, M.; Jorda, M.; Vardoulis, O.; Chortos, A.; Khatib, O.; Bao, Z. A Hierarchically Patterned, Bioinspired E-Skin Able to Detect the Direction of Applied Pressure for Robotics. *Sci. Rob.* **2018**, *3*, No. eaau6914.

(31) Xu, H.; Lv, Y.; Qiu, D.; Zhou, Y.; Zeng, H.; Chu, Y. An Ultra-Stretchable, Highly Sensitive and Biocompatible Capacitive Strain Sensor from an Ionic Nanocomposite for On-Skin Monitoring. *Nanoscale* **2019**, *11*, 1570–1578.

(32) Dickey, M. D. Stretchable and Soft Electronics using Liquid Metals. *Adv. Mater.* **2017**, *29*, No. 1606425.

(33) Guo, R.; Tang, J.; Dong, S.; Lin, J.; Wang, H.; Liu, J.; Rao, W. One-Step Liquid Metal Transfer Printing: Toward Fabrication of Flexible Electronics on Wide Range of Substrates. *Adv. Mater. Technol.* **2018**, *3*, No. 1800265.

(34) Zhu, S.; So, J.-H.; Mays, R.; Desai, S.; Barnes, W. R.; Pourdeyhimi, B.; Dickey, M. D. Ultrastretchable Fibers with Metallic Conductivity Using a Liquid Metal Alloy Core. *Adv. Funct. Mater.* **2013**, *23*, 2308–2314.

(35) Wang, J.; Cai, G.; Li, S.; Gao, D.; Xiong, J.; Lee, P. S. Printable Superelastic Conductors with Extreme Stretchability and Robust Cycling Endurance Enabled by Liquid-Metal Particles. *Adv. Mater.* **2018**, *30*, No. 1706157.

(36) Chechetka, S. A.; Yu, Y.; Zhen, X.; Pramanik, M.; Pu, K.; Miyako, E. Light-Driven Liquid Metal Nanotransformers for Biomedical Theranostics. *Nat. Commun.* **2017**, *8*, No. 15432.

(37) Wang, X.; Yao, W.; Guo, R.; Yang, X.; Tang, J.; Zhang, J.; Gao, W.; Timchenko, V.; Liu, J. Soft and Moldable Mg-Doped Liquid Metal for Conformable Skin Tumor Photothermal Therapy. *Adv. Healthcare Mater.* **2018**, *7*, No. 1800318.

(38) Guo, R.; Liu, J. Implantable Liquid Metal-Based Flexible Neural Microelectrode Array and Its Application in Recovering Animal Locomotion Functions. *J. Micromech. Microeng.* **2017**, *27*, No. 104002.

(39) Kim, S.; Oh, J.; Jeong, D.; Bae, J. Direct Wiring of Eutectic Gallium-Indium to a Metal Electrode for Soft Sensor Systems. *ACS Appl. Mater. Interfaces* **2019**, *11*, 20557–20565.

(40) Li, G.; Lee, D. W. An Advanced Selective Liquid-Metal Plating Technique for Stretchable Biosensor Applications. *Lab Chip* **2017**, *17*, 3415–3421.

(41) Li, G.; Wu, X.; Lee, D.-W. Selectively Plated Stretchable Liquid Metal Wires for Transparent Electronics. *Sens. Actuators, B* **2015**, *221*, 1114–1119.

(42) Wang, L.; Liu, J. Pressured Liquid Metal Screen Printing for Rapid Manufacture of High Resolution Electronic Patterns. *RSC Adv.* **2015**, *5*, 57686–57691.

(43) Park, C. W.; Moon, Y. G.; Seong, H.; Jung, S. W.; Oh, J. Y.; Na, B. S.; Park, N. M.; Lee, S. S.; Im, S. G.; Koo, J. B. Photolithography-Based Patterning of Liquid Metal Interconnects for Monolithically Integrated Stretchable Circuits. *ACS Appl. Mater. Interfaces* **2016**, *8*, 15459–15465.

(44) Qusba, A.; RamRakhyani, A. K.; So, J.-H.; Hayes, G. J.; Dickey, M. D.; Lazzi, G. On the Design of Microfluidic Implant Coil for Flexible Telemetry System. *IEEE Sens. J.* **2014**, *14*, 1074–1080.

- (45) Park, Y.-L.; Majidi, C.; Kramer, R.; Bérard, P.; Wood, R. J. Hyperelastic Pressure Sensing with a Liquid-Embedded Elastomer. *J. Micromech. Microeng.* **2010**, *20*, No. 125029.
- (46) Tang, L.; Cheng, S.; Zhang, L.; Mi, H.; Mou, L.; Yang, S.; Huang, Z.; Shi, X.; Jiang, X. Printable Metal-Polymer Conductors for Highly Stretchable Bio-Devices. *iScience* **2018**, *4*, 302–311.
- (47) Mohammed, M. G.; Kramer, R. All-Printed Flexible and Stretchable Electronics. *Adv. Mater.* **2017**, *29*, No. 1604965.
- (48) Mengüç, Y.; Park, Y.-L.; Pei, H.; Vogt, D.; Aubin, P. M.; Winchell, E.; Fluke, L.; Stirling, L.; Wood, R. J.; Walsh, C. J. Wearable Soft Sensing Suit for Human Gait Measurement. *Int. J. Rob. Res.* **2014**, *33*, 1748–1764.
- (49) Dellon, E. S.; Mourey, R.; Dellon, A. L. Human Pressure Perception Values for Constant and Moving One-and Two-Point Discrimination. *Plast. Reconstr. Surg.* **1992**, *90*, 112–117.
- (50) Qiu, Z.; Wan, Y.; Zhou, W.; Yang, J.; Yang, J.; Huang, J.; Zhang, J.; Liu, Q.; Huang, S.; Bai, N.; Wu, Z.; Hong, W.; Wang, H.; Guo, C. F. Ionic Skin with Biomimetic Dielectric Layer Templated from *Calathea Zebrina* Leaf. *Adv. Funct. Mater.* **2018**, *28*, No. 1802343.
- (51) Machaly, S. A.; Senna, M. K.; Sadek, A. G. Vertigo is Associated with Advanced Degenerative Changes in Patients with Cervical Spondylosis. *Clin. Rheumatol.* **2011**, *30*, 1527–1534.